Journal of Materials Chemistry C

Accepted Manuscript

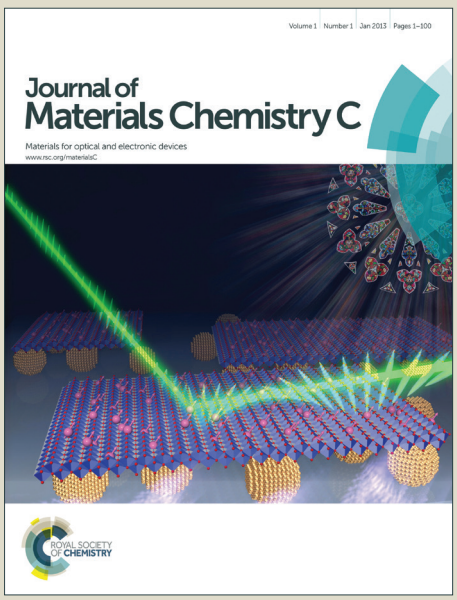

ROYAL SOCIETY OF CHEMISTRY

www.rsc.org/materialsC

Synthesis of highly fluorescent P, O-g-C_3N_4 nanodots for the label-free detection of Cu^{2+} and acetylcholinesterase activity

Mingcong Rong[a], Xinhong Song[a], Tingting Zhao[c], Qiuhong Yao[c], Yiru Wang[a], Xi Chen[a,b]*

[a]Department of Chemistry and the MOE Key Laboratory of Spectrochemical Analysis & Instrumentation, College of Chemistry and Chemical Engineering, Xiamen University, Xiamen 361005, China

[b]State Key Laboratory of Marine Environmental Science, Xiamen University, Xiamen, 361005, China

[c]Xiamen Huaxia University, Xiamen, 361005, China

Abstract: Highly fluorescent phosphorus, oxygen-doped graphitic carbon nitride nanodots (P, O-g-C_3N_4 nanodots) were synthesized using chemical oxidation and hydrothermal etching of bulk P-g-C_3N_4 obtained via pyrolysis of phytic acid and melamine. The P, O-g-C_3N_4 nanodots emitted strong blue fluorescence with a high quantum yield of 90.2%, and displayed high resistance to photobleaching and high ionic strength. A sensitive and facile fluorescence sensing approach for Cu^{2+} was developed through fluorescence quenching based on the static fluorescence quenching and photoinduced electron transfer. Under optimal conditions, a rapid detection of Cu^{2+} could be completed in 5 min with a detection limit of 2 nM, and a linearity ranging from 0 to 1 μM. Using acetylthiocholine (ATCh) as the substrate, the fluorescence of the P, O-g-C_3N_4 nanodots-Cu^{2+} system could be sensitively turned on in the presence of acetylcholinesterase (AChE) through the reaction between Cu^{2+} and thiocholine, the hydrolysis product of ATCh by AChE. A linearity ranging from 0.01 to 3 mU/mL could be obtained with a detection limit of 0.01 mU/mL. In addition, the proposed approach showed potential application for the detection of Cu^{2+} in natural

* Corresponding author. Tel: +86 592 2184530; Fax: +86 592 2184530; E-mail address: *xichen@xmu.edu.cn*

water samples and AChE activity in human plasma.

Introduction

Graphitic carbon nitride (g-C_3N_4), a well-known graphene-like carbon-based material, receives much attention because of its special structure and properties.[1] Since g-C_3N_4 is a chemically and thermally stable metal-free semiconductor with a bandgap of 2.7 eV, it is explored in a variety of applications, especially in the fields of photoelectrocatalysis, photovoltaic solar cells and the oxygen reduction reaction.[2-5] Nanoscale g-C_3N_4 materials, such as fluorescent g-C_3N_4 nanosheets and g-C_3N_4 nanodots/quantum dots, draw great attention in sensing[6-8], bioimaging[9,10] and peroxidase-like catalysis[11-13] because of their excellent optical and physicochemical features, including high photostability, resistance against photobleaching, high quantum yield, low cost, good water solubility and biological compatibility.[14,15] At present, the available methods for the synthesis of g-C_3N_4 nanodots include microwave-assisted or hydrothermal polymerization of organic molecules with high nitrogen content and hydrothermal etching of bulk g-C_3N_4.[16-18] For bulk g-C_3N_4, heteroatom (B, O, F, P, S, I) doping is an effective and common way to modify and improve their photocatalysis properties.[19-24] However, it is rarely used in the optical property modulation of g-C_3N_4 nanodots, in addition to O, S-doping.[15] There is still a large gap in quantum yield between the (heteroatom doping) g-C_3N_4 nanodots and highly fluorescent CdSe quantum dots, and even some heteroatom-doped carbon dots. Therefore, the exploration of novel, highly fluorescent, heteroatom doped-g-C_3N_4 nanodots is eagerly anticipated.

Nowadays, with rapid industrial development, environmental pollution has become a serious problem, and the detection of toxic metals in environmental monitoring and clinical research is a significant issue. Copper (Cu) is a widely used industrial metal and it is an essential trace element in various biological processes.[25] The excess accumulation of Cu^{2+} in the human body causes damage to the central nervous system and induces neurodegenerative diseases such as Alzheimer's disease, Menkes syndrome, amyotrophic lateral sclerosis and Wilson's disease.[7,26] Currently, a number

of fluorescent materials have been developed for the determination of Cu^{2+}, including noble metal nanoclusters,[27] semiconductor quantum dots,[28] small organic molecules[29] and iridium complexs.[30,31] However, these methods suffer drawbacks such as expensive cost, high toxicity, and photobleaching, which limit their widespread application. Although there are some attractive fluorescence sensors using carbon nanomaterials,[7,17,25] it is still essential to develop more simple, rapid and highly sensitive detection methods for Cu^{2+}.

Acetylcholinesterase (AChE) is a type of serine esterase in the central and peripheral nervous systems, which regulates the levels of the neurotransmitter acetylthiocholine (ATCh) by catalyzing the hydrolysis reaction of ATCh to choline.[26,32] Many neurodegenerative diseases including Alzheimer's disease and Parkinson's disease are related to the degeneration of the cholinergic system, resulting in decreased amounts of AChE and ATCh.[33] Therefore, great efforts have been made to detect the activity of AChE. The classical method, Ellman's colorimetry technique, is limited by its low sensitivity.[26] Other feasible methods contain fluorescent UCNP-Au nanoparticles,[34] CdS quantum dots,[35] and noble Au nanoclusters.[36] However, some disadvantages still exist, such as complicated synthesis, high toxicity, expensive cost and long measurement time. Hence, novel label-free, economic, time-saving, highly sensitive and selective methods are urgently needed.

In our work, highly fluorescent P, O-g-C_3N_4 nanodots were obtained through chemical oxidation and hydrothermal etching of bulk P-g-C_3N_4 using melamine as a precursor and phytic acid as a phosphorus dopant. The as prepared P, O-g-C_3N_4 nanodots emitted strong blue fluorescence with a high quantum yield of 90.2%, which is almost the highest among previously reported g-C_3N_4 nanodots/quantum dots. They displayed high resistance to photobleaching and high ionic strength. Using the P, O-g-C_3N_4 nanodots, we developed a label-free, sensitive and selective sensing approach for the fluorescence "on-off" detection of Cu^{2+} in aqueous solution via static fluorescence quenching and photoinduced electron transfer (PET) from them to Cu^{2+}. In the meantime, ATCh could be hydrolyzed into thiocholine (TCh) and displace the P, O-g-C_3N_4 nanodots to form the Cu(I)-TCh complex in the presence of AChE. As a

result, the fluorescence of the P, O-g-C_3N_4 nanodots-Cu^{2+} system was restored in an "off-on" way for the detection of AChE activity. The proposed approach provided a low detection limit for both Cu^{2+} and AChE and showed its applicability to natural water samples spiked with Cu^{2+} and to AChE activity in human plasma.

Experimental section

Materials

Melamine was purchased from the Tianjin Guangfu Fine Chemical Research Institute (Tianjin, China). Phytic acid, AChE (from *Elcetrophorus electricus*, 1000 U/mg, the total activity is 500 U, 0.5 mg), acetylthiocholine (ATCh), lysozyme, trypsin, pepsin, bovine serum albumin (BSA), glutathione (GSH), L-cysteine (Cys), homocysteine (Hcy), nafion (5 wt.% in H_2O) , ferrocene and tera-n-butylammonium hexafluorophostate were obtained from Sigma-Aldrich (Shanghai, China), and horseradish peroxidase (HRP) was from the Sangon Biotech Co., Ltd. (Shanghai, China). All metal nitrates or chlorides of analytical grade were purchased from the Sinopharm Chemical Reagent Co., Ltd. (Shanghai, China). Healthy human plasmas were obtained from the First Affiliated Hospital of Xiamen University (Xiamen). All chemicals were of analytical grade and used as received without further purification. All solutions were prepared using ultrapure water with a resistivity of 18.2 $M\Omega \cdot cm^{-1}$ from a Millipore purification system (Millipore, USA). All procedures involving human plasma were conducted with the approval of the First Affiliated Hospital of Xiamen University (Xiamen) and Xiamen University.

Instrumentation

UV–Vis absorption and fluorescence spectra were performed with a UV2550 spectrophotometer (Shimadzu, Japan) and F-7000 spectrophotometers (Hitachi, Japan). Fourier transform infrared (FT-IR) spectra were obtained from a Nicolet 380 spectrophotometer (Thermo Electron Corp., U.S.A.), and the fluorescence lifetime was measured using a FluoroMax-4 spectrofluorometer (Horiba JobinYvon, France). Transmission electron microscope (TEM) and atomic force microscope (AFM) images were collected from a TECNAI F30 (Philips-FEI, Netherlands) at an

acceleration voltage of 300 kV and a 5500 SPM (Agilent, America) with silicon probes. X-ray powder diffraction (XRD) results were obtained from a Rigaku Ultima IV XRD diffractometer (Rigaku, Japan) equipped with graphite monochromatized high-intensity Cu-Ka radiation (λ = 1.5417 Å). X-ray photoelectron spectroscopy (XPS) was measured using a PHI Quantum 2000 XPS system (Physical Electronics, U.S.A.) with Al Kα (hυ = 1486.60 eV). Inductively coupled plasma mass spectroscopy (ICP-MS) was performed with a DRC II 2000 ICP-MS instrument (PerkinElmer, USA).

Preparation of the P, O-g-C_3N_4 nanodots

The bulk P-g-C_3N_4 was prepared based on previous reports with minor modification.[37] First, a phytic acid-melamine complex was prepared using a 1:10 mass ratio of phytic acid and melamine (5.0 g total weight) in 40 mL water. Then, the complex was blended for 4 h using an oscillator, and the obtained complex was dried at 60 °C in an oven and then transferred to a tube furnace. The complex was calcined for 3 h to 550 °C, maintaining it for another 4 h under nitrogen conditions to gain the bulk P-g-C_3N_4. Secondly, 300 mg of the finely ground bulk P-g-C_3N_4 power was added into 30 mL of 5 M HNO_3 and refluxed at 120 °C for 24 h. After cooling to room temperature, the refluxed P-g-C_3N_4 was centrifuged at 10 000 rpm for 30 min and then washed three times with ultrapure water to neutral, and the mixture were centrifuged to retain the sediment. Finally, 150 mg of the chemically oxidized P-g-C_3N_4 (the sediment) was dispersed in 15 mL ultrapure water, then transferred into a 25 mL Teflon cup and heated in a sealed autoclave at 200 °C for 20 h. After cooling to room temperature, the obtained supernatant was filtered through a 0.22 μm water phase microporous membrane filter, and dialyzed in a dialysis bag (MWCO:14 k) to remove large-sized nanoparticles. The concentration of the as prepared P, O-g-C_3N_4 nanodots was 280 μg/mL.

Fluorescence sensing of Cu^{2+}

10 μL of the as prepared P, O-g-C_3N_4 nanodots were mixed with a 10 mM borate buffer solution (pH 7.0) containing different concentrations (0 to 20 μM) of Cu^{2+}. The final volume of the solution was kept at 1.0 mL. After 5 min of reaction at room

temperature, the fluorescence spectra of the solutions were collected in the wavelength range from 370 to 600 nm (the excitation wavelength was 350 nm; both excitation and emission slits were 5 nm).

In the investigation of the selectivity of Cu^{2+}, several coexisting metal ions were selected and the concentration of all ions was 1 μM. The same detection conditions were selected as mentioned above.

In the determination of Cu^{2+} in a lake water sample, the water sample was obtained from Xiamen University campus. The sample was centrifuged at 12 000 rpm for 30 min twice and then the supernatant filtered through a 0.22 μm water phase membrane. 10 μL of the as prepared P, O-g-C_3N_4 nanodots were mixed with a 10 mM borate buffer solution (pH 7.0) containing different concentrations (0, 0.1, 0.25, 0.5, 0.75 and 1 μM) of Cu^{2+} and 500 μL lake water sample. The same detection conditions were selected as mentioned above.

Time-resolved decay measurements were investigated to explore the reaction mechanism between the P, O-g-C_3N_4 nanodots and Cu^{2+}. 10 μL of the as prepared P, O-g-C_3N_4 nanodots were mixed with a 10 mM borate buffer solution (pH 7.0) containing different concentrations (0, 0.1, 1, 5 and 10 μM) of Cu^{2+}. The final volume of the solution was kept as 1.0 mL. The excitation wavelength was 339 nm (the closest to 350 nm), and the emission wavelength was 440 nm.

Fluorescence sensing of AChE activity

20 μL borate buffer solution (100 mM, pH 7.0) was mixed with 100 μL 10 mM ATCh, and different concentrations of AChE in a final volume of 200 μL. The mixture was incubated at 37 °C for 30 min, and then 80 μL 100 mM borate buffer solution (pH 7.0), 10 μL of the as prepared P, O-g-C_3N_4 nanodots and 790 μL ultrapure water containing 15 nmol Cu^{2+} were added to a final volume of 1 mL. The mixture was incubated at room temperature for 5 min before the fluorescence spectra were collected.

In the investigation of the selectivity of AChE activity, several coexisting enzymes and substances were selected. The concentration of AChE was 10 mU/mL (equals to 10 μg/L). The concentration of all enzymes except HRP was 10 mU/mL and the

concentration of GSH, Cys, Hcy, BSA, HRP and other ions was 1 μM. The same detection conditions were selected as mentioned above.

In the determination of AChE activity in biological fluids samples, healthy human plasma samples were diluted 200-fold before determination. 20 μL borate buffer solution (100 mM, pH 7.0) was mixed with 100 μL 10 mM ATCh, and 10 μL of the diluted human plasma was added in a final volume of 200 μL. The following treatment methods were the same as those for the sensing of AChE activity.

Results and discussion

Characterization of materials

Melamine was used as a precursor of g-C_3N_4 because of its low cost, abundance and nitrogen-rich characteristics. Phytic acid is a natural and environmental organic phosphate compound with six phosphate groups. Its special structure made it a multi-complexing agent for metal ions and an ideal candidate for phosphorus-doping because of the rich content of phosphorus.[38] The acid-base interaction between melamine and phytic acid can facilitate their cross-linking. The P, O-g-C_3N_4 nanodots were prepared by chemical oxidation and hydrothermal etching of bulk P-g-C_3N_4 produced by the polymerization of melamine and phytic acid at high temperature. The morphologies of bulk P-g-C_3N_4 and the P, O-g-C_3N_4 nanodots were characterized using SEM and TEM. As shown in Figure 1 A and B, the bulk P-g-C_3N_4 consists of irregular folded flakes approximately several micrometers in size. In contrast, the P, O-g-C_3N_4 nanodots were mono-dispersed in a narrow diameter range from 4 to 12 nm and mainly located at about 6 nm. The corresponding AFM image revealed a thickness of the P, O-g-C_3N_4 nanodots in the range 3.51 to 4.15 nm (Figure 1C), which indicated that the as-prepared P, O-g-C_3N_4 nanodots comprised 10 to 12 layers of C-N sheets. The XRD patterns of the bulk P-g-C_3N_4 and the P, O-g-C_3N_4 nanodots were shown in Figure 1D, and revealed that there were two prominent peaks at 13.0° and 27.3°. The strong characteristic peak at 27.3° corresponded to the typical graphitic interlayer stacking (002) peak of g-C_3N_4. The smaller peak at 13.0° corresponded to the periodic in-plain structural packing feature within the sheets. The

peak at 13.0° disappeared in the P, O-g-C_3N_4 nanodots and so revealed its size decrease.[14,39] The composition and structure of the P, O-g-C_3N_4 nanodots were further explored using FT-IR, XPS measurements and elemental analysis. As displayed in Figure S2, the peaks at 811 cm^{-1} and between 1000 to 1800 cm^{-1} were attributed to the triazine ring and CN heterocycles. In addition, the peak from 3000 to 3600 cm^{-1} corresponded to N-H and O-H. The new peaks at 950, 1072 and 1115 cm^{-1} revealed the stretching mode of P-N and the increased content of C-O and C=O, and the peak shifts from 3140 to 3429 cm^{-1} also indicated the increased content of O-H and the reduced content of N-H.[22,40] The elemental analysis showed a N/C ratio of 1.55 in the bulk P-g-C_3N_4 to 1.46 in the P, O-g-C_3N_4 nanodots and a great loss of both C and N element content in the P, O-g-C_3N_4 nanodots, the N/C ration can also imply the maintaining of C_3N_4 structure.(Table S1) As shown in Figure S3, the contents of the major chemical elements (C, N, O, P) changed from a ratio of 0.491/0.4784/0.0247/0.0059 in the bulk P-g-C_3N_4 to 0.3668/0.0731/0.5283/0.0317 in the P, O-g-C_3N_4 nanodots. The discrepancy of element content between XPS measurements and element analysis may be ascribed to their different test subject, element analysis refers to the whole material and XPS measurements refers to the functional groups on the surface of the material. The increase of oxygen content and the decrease of nitrogen content of the P, O-g-C_3N_4 nanodots may have been caused by the generation of oxygen-containing groups and the degradation of the nitrogenous group on a few superficial layers of the P, O-g-C_3N_4 nanodots during the synthesis process, while the inside layers remain the structure of bulk P-g-C_3N_4. The C 1s spectrum showed three peaks centering at 284.8, 286.6, 288.0 or 288.8 eV, which could be attributed to graphitic carbon, C-O, N-C=N and C=N, C=O bonds. The N 1s spectrum revealed four peaks centering at 398.4, 399.5, 401.0 and 407.0 eV, corresponding to C=N-C, N-(C)3, C-NH bonds and charging effects or positive charge localization in CN heterocycles.[39] The O 1s spectrum demonstrated two peaks centering at 531.1 and 532.5 eV, ascribed to N-C=O and C-OH.[14] The P 2p spectrum showed three peaks centering at 133.6, 134.0 and 135.0 eV, attributed to P-N, P=N and P-O bonds.[22,40,41] All the results confirmed that the P, O-g-C_3N_4 nanodots retained

the g-C_3N_4 structure, and revealed the existence of oxygen-rich groups, and that P was probably doped into the g-C_3N_4 structure by replacing C in the P, O-g-C_3N_4 nanodots.

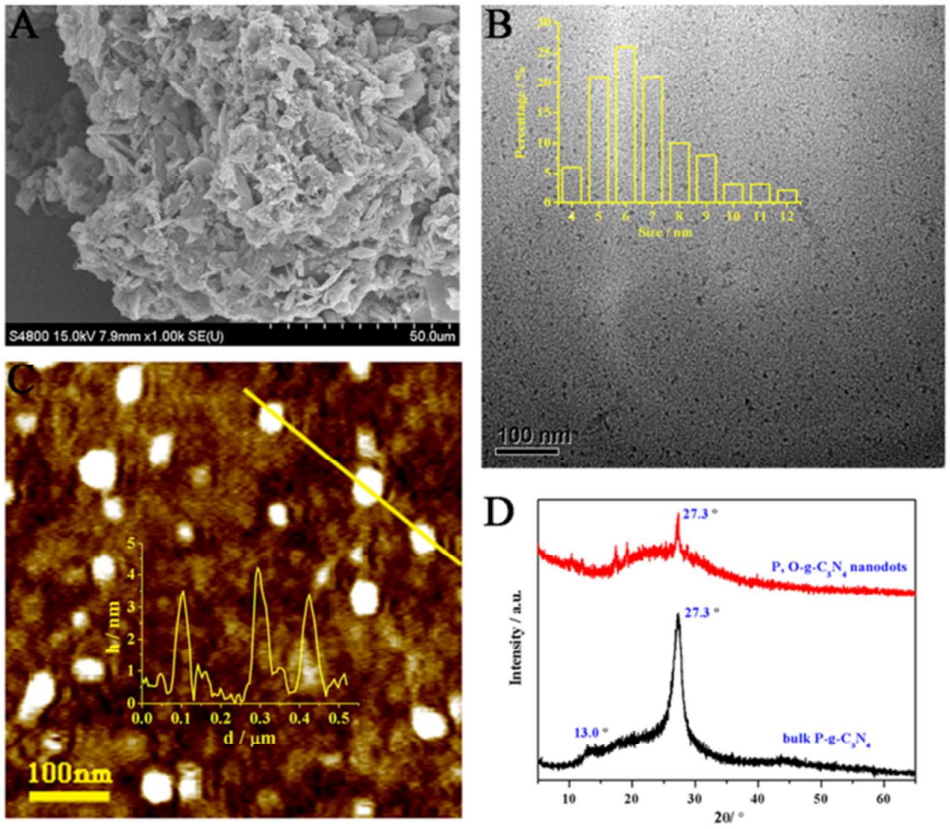

Figure 1. (A) SEM image of the bulk P-g-C_3N_4. (B) TEM image of the P, O-g-C_3N_4 nanodots (inset shows the corresponding size distribution of the P, O-g-C_3N_4 nanodots). (C) AFM image of the P, O-g-C_3N_4 nanodots (inset shows the corresponding height of the P, O-g-C_3N_4 nanodots). (D) XRD patterns of the bulk P-g-C_3N_4 and the P, O-g-C_3N_4 nanodots.

In our study, we found that the strong fluorescence emission of the P, O-g-C_3N_4 nanodots could be efficiently turned off by Cu^{2+} owing to the chelation of Cu^{2+} with N in the P, O-g-C_3N_4 nanodots via static fluorescence quenching and the PET from the P, O-g-C_3N_4 nanodots to Cu^{2+}. In the meantime, the fluorescence of the P, O-g-C_3N_4 nanodots-Cu^{2+} system could be effectively turned on in the presence of AChE and ATCh through the reaction of Cu^{2+} and TCh, the hydrolysis product of ATCh by AChE. The possible mechanism is illustrated in Scheme 1B.

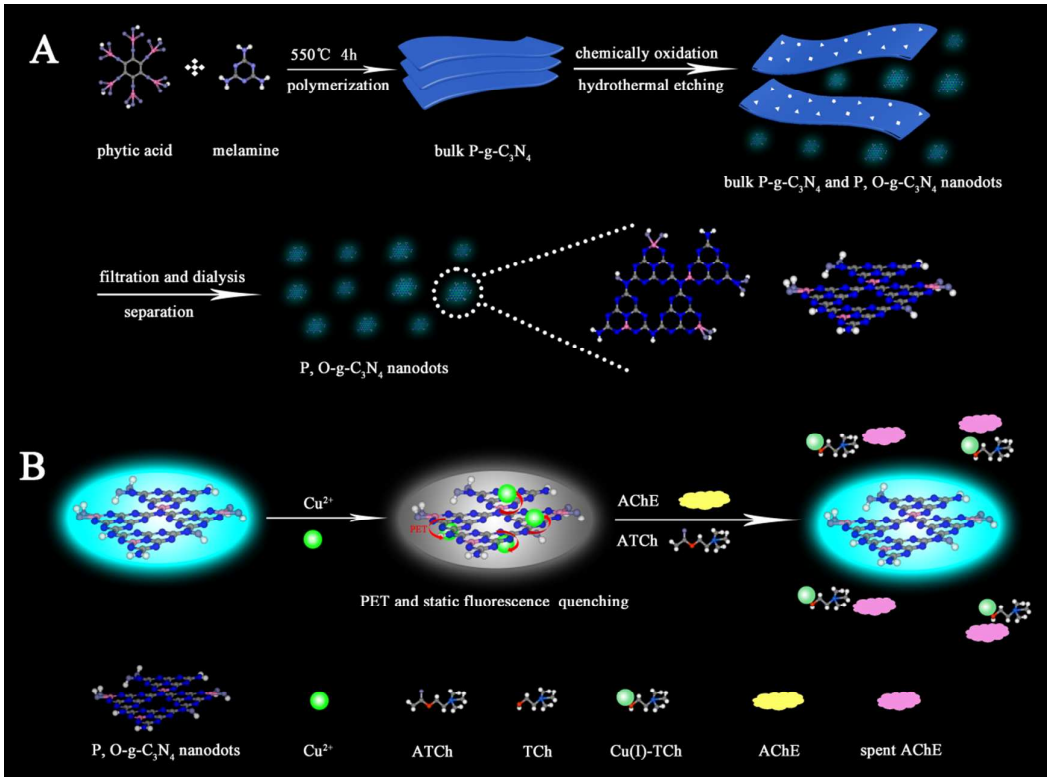

Scheme 1. (A) The Synthesis of Fluorescent P, O-g-C_3N_4 Nanodots. (B) Schematic Illustration of the Sensitive and Selective Fluorescence Detection of Cu^{2+} and AChE Activity Based on the P, O-g-C_3N_4 Nanodots

Spectroscopic properties of the P, O-g-C_3N_4 nanodots

The P, O-g-C_3N_4 nanodots exhibited excellent solubility in water and the solution was stable for six months at 4 °C without any precipitation. The optical properties of the P, O-g-C_3N_4 nanodots were characterized by UV-vis absorption and fluorescence spectra. As shown in Figure 2A, they presented a shoulder absorption peak at 252 and 350 nm. The peak at 252 nm was contributed by π-π* electronic transitions for carbon nitrides containing s-triazine rings,[18] and the peak at 350 nm indicated the n-π* electronic transitions of C=N and C=O in the P, O-g-C_3N_4 nanodots.[42] Under an excitation of 350 nm, the P, O-g-C_3N_4 nanodots exhibited a strong emission at 440 nm. A shoulder emission at 400 nm could be caused by the transition between the long pair valence band and the δ* conduction band which is related to the sp^2 C-N band.[43] The fluorescence emission of the P, O-g-C_3N_4 nanodots was found to be excitation

dependent (Figure 2B), just as in a previous report of g-C_3N_4 quantum dots.[18] The fluorescence emission peak shifted from 400 to 450 nm when the excitation wavelength changed from 300 to 390 nm. The fluorescence properties of the P, O-g-C_3N_4 nanodots were further investigated using quantum yield and the effects of external factors. Under an excitation of 350 nm, the quantum yield of the P, O-g-C_3N_4 nanodots was 90.2% using quinine sulfate as a reference (Figure S1). The luminescence of the P, O-g-C_3N_4 nanodots may be ascribed to the π-π*、n-π* electronic transitions in the C=N, C=O structure and the photogeneration of electron-hole pairs that induce radiative recombination of the trap carriers localized in the P, O-doped s-triazine rings and the recombination of photogenerated charges on the surface defects. The high quantum yield of the P, O-g-C_3N_4 nanodots may be caused by the n-π* transition from increased C=O, P-O, C-OH groups, which effectively suppress non-radiative recombination of localized electron-hole pairs and enhance the intrinsic and surface defects state emission.[43-46] The detail mechanism of their high quantum yield is under careful study. The P, O-g-C_3N_4 nanodots also exhibited high photostability and resistance to high ionic strength. As shown in Figures 2D and S4, the fluorescence intensity of the P, O-g-C_3N_4 nanodots remained constant after continuous irradiation for 2 h and scarcely showed a fluorescence intensity change in 1 M NaCl solution. These results indicated the potential application of P, O-g-C_3N_4 nanodots in fluorescence imaging and physiological conditions.

In order to obtain the optimal conditions for further analytical applications, the effects of pH and the concentration of the P, O-g-C_3N_4 nanodots were investigated. The fluorescence intensity of the P, O-g-C_3N_4 nanodots remained constant from pH 5.5 to 9.5 (Figure 2C). Based on the results in Figure S5, 10 μL of the stock solution of the P, O-g-C_3N_4 nanodots (2.8 μg/mL) was selected and applied in the following experiments.

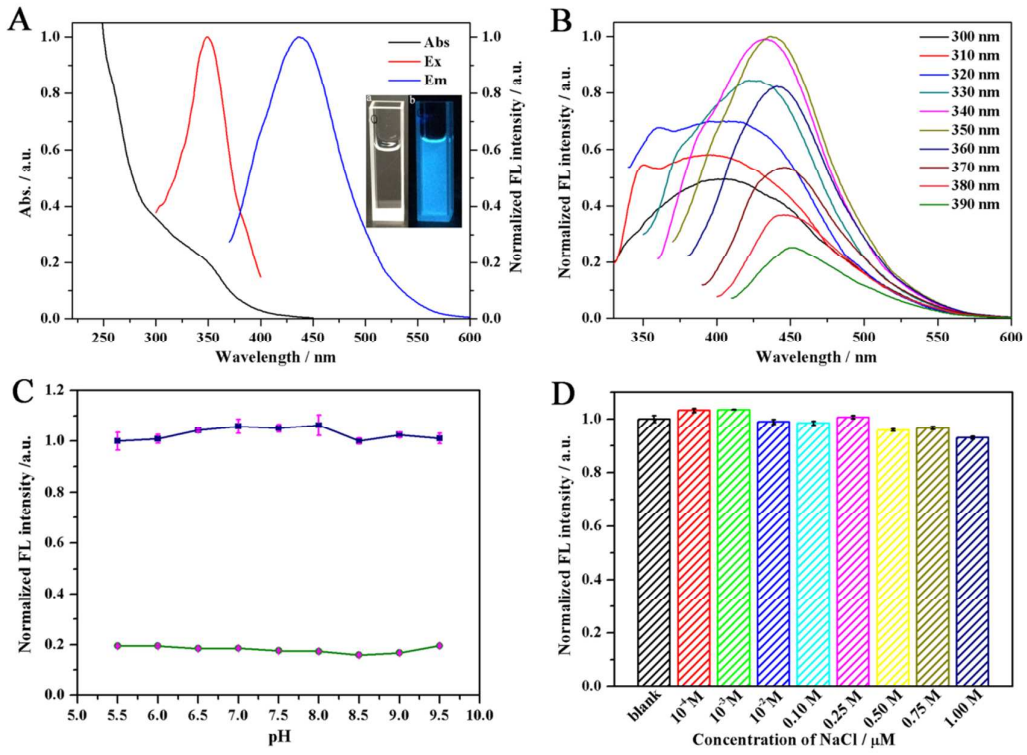

Figure 2. (A) UV-vis absorption and fluorescence excitation and emission spectra of the P, O-g-C_3N_4 nanodots. Inset: photographs of the solution of P, O-g-C_3N_4 nanodots under (a) daylight and (b) 365 nm UV light. (B) The emission spectra of the P, O-g-C_3N_4 nanodots under different excitation wavelengths ranging from 300 to 390 nm. (C) Fluorescence responses of the P, O-g-C_3N_4 nanodots in the absence and presence of 3 μM Cu^{2+} in different pH solutions (10 mM borate buffer). (D) Stability of the P, O-g-C_3N_4 nanodots in the presence of different concentrations of NaCl.

Determination of Cu^{2+} using the P, O-g-C_3N_4 nanodots

The analytical performance of the P, O-g-C_3N_4 nanodots was evaluated. Cu^{2+} is one of the best quenchers to fluorescent g-C_3N_4.[7,47,48] In the experiments, we explored the feasibility of the P, O-g-C_3N_4 nanodots for Cu^{2+} detection. Figure 3A displays the fluorescence responses of the P, O-g-C_3N_4 nanodots at 440 nm in the absence and presence of Cu^{2+}. The addition of Cu^{2+} led to a quick (within 5 min) and significant decrease in the fluorescence intensity of the P, O-g-C_3N_4 nanodots (Figure S6), which indicated that the P, O-g-C_3N_4 nanodots could be an effective sensing nanomaterial

for Cu^{2+} detection. In order to obtain a better detection performance, the effect of pH was also examined. As shown in Figure 2C, the fluorescence quenching efficiency remained stable from pH 5.5 to 9.5, indicating the potential applications of using these nanodots under some physiological and environmental conditions. In the following experiments, the detections were carried out in neutral pH. Consequently, all the following experiments were carried out at pH 7.0 with a reaction time of 5 min. In the sensitivity study, the fluorescence response of different concentrations of Cu^{2+} in the range 0 to 20 μM was investigated. Figure 3A shows that the fluorescence intensity of the P, O-g-C_3N_4 nanodots gradually decreased with the increase of Cu^{2+} concentration, which indicated the high sensitivity of the P, O-g-C_3N_4 nanodots towards Cu^{2+}. The inset figure in Figure 3B reveals a good linearity between the fluorescence intensity and the Cu^{2+} concentration from 0 to 1 μM, with a detection limit of 2 nM at a signal-to-noise ratio of 3. And the fluorescence of the P, O-g-C_3N_4 nanodots can be fully quenched with 15 μM Cu^{2+}. The fluorescence intensity versus the concentration of Cu^{2+} could be fitted to a linear equation of $F/F_0 = 1.955\ [Cu^{2+}]\ (\mu M) + 0.9440$, with a correlation coefficient R of 0.9911. According to the US Environmental Protection Agency, the maximum concentration of Cu^{2+} in drinking water should be no more than 20 μM, indicating that the proposed approach is sensitive enough to monitor Cu^{2+} in drinking water.[26]

To evaluate the selectivity of the P, O-g-C_3N_4 nanodots towards Cu^{2+}, the effects of the co-existing ions were investigated under the same conditions. The results in Figure 3C reveal that other ions showed ignorable interference for Cu^{2+} determination within the linearity range. The application of the Cu^{2+} sensing was investigated in natural water samples. A recovery study was carried out on the samples spiked with different concentration Cu^{2+} solutions, and the results, listed in Table 1, showed recoveries from 101 to 118%. The results matched well with those obtained from ICP-MS, indicating the applicability of the proposed methods to natural water samples. A comparison of the sensing performance of different fluorescence sensing approaches for Cu^{2+} is shown in Table S2. The results indicated that the proposed method was fast, sensitive and facile among the previously reported sensing systems.

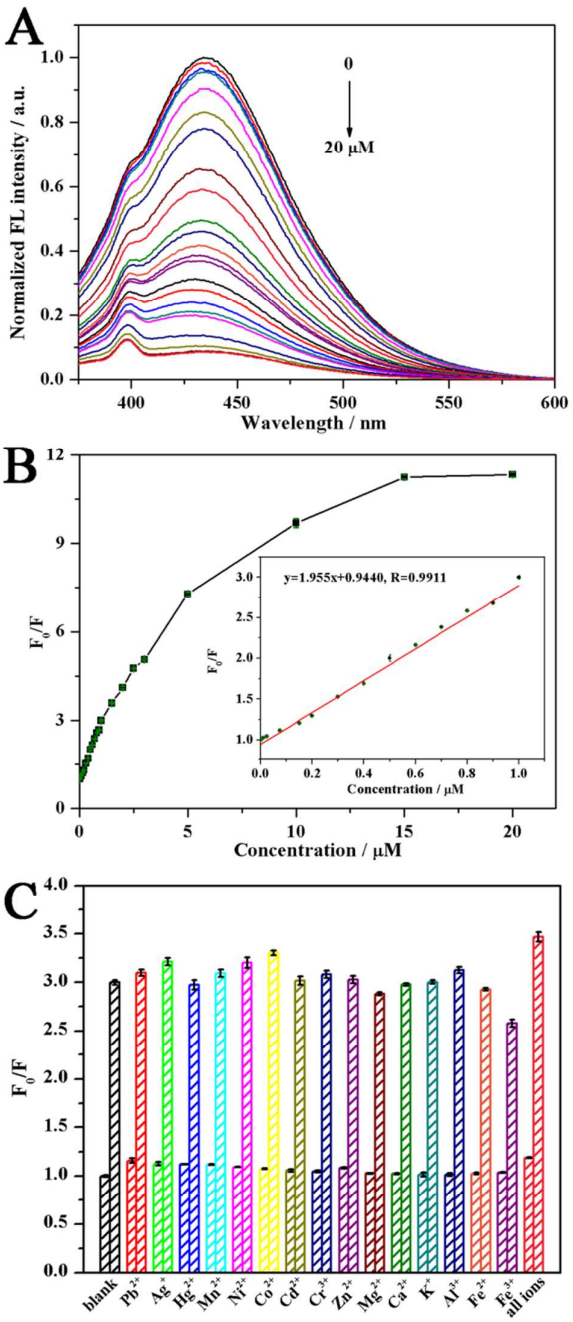

Figure 3. (A) Fluorescence responses of the P, O-g-C_3N_4 nanodots in the presence of increasing concentrations of Cu^{2+} (0, 0.005, 0.01, 0.025, 0.075, 0.15, 0.2, 0.3, 0.4, 0.5, 0.6, 0.7, 0.8, 0.9, 1, 1.5, 2, 2.5, 3, 5, 10, 15, 20 μM) in 10 mM borate buffer (pH 7.0). (B) The relationship between F_0/F and the concentration of Cu^{2+}. The inset figure presents the linear responses to Cu^{2+} ranging from 0 to 1 μM. (C) Fluorescence responses of the P, O-g-C_3N_4 nanodots in the presence of 1 μM of various ions

solutions. F_0 and F represent the fluorescence intensities of the P, O-g-C_3N_4 nanodots at 440 nm in the absence and presence of Cu^{2+} or other ions.

Table 1. Determination of Cu^{2+} spiked in natural water samples (n=3)

Concentration added (nM)	Concentration found (nM)	Recovery %	RSD %	Concentration found using ICP-MS (nM)
0	20.5	/	1.68	27.1
100	118	118	1.53	125
250	271	108	1.75	275
500	513	103	1.61	520
750	760	101	1.12	766
1000	1008	101	1.45	1017

Recovery% = 100% × (concentration found / concentration added)

In order to verify the detection mechanism of the P, O-g-C_3N_4 nanodots towards Cu^{2+}, we explored the fluorescence lifetime of the P, O-g-C_3N_4 nanodots with several different concentrations of Cu^{2+}. As shown in Figure S7, the lifetime gradually decreased with the increase of Cu^{2+} concentration, which indicated the existence of dynamic fluorescence quenching of the P, O-g-C_3N_4 nanodots towards Cu^{2+}. At the same time, the broader and sharper FT-IR band from 1072 to 1115 cm^{-1} and from 2800 to 2900 cm^{-1} in Figure S2 also proved the chelation of Cu^{2+} with N in the P, O-g-C_3N_4 nanodots and formation of the P, O-g-C_3N_4 nanodots-Cu^{2+} complex.[25] Because the redox potential of Cu^{2+}/Cu^{+} lies between the conduction band and valence band of the P, O-g-C_3N_4 nanodots (the details were illustrated in Figure S8), PET from the conduction band of the P, O-g-C_3N_4 nanodots to the Cu^{2+} in close proximity will lead to fluorescence quenching.[7] However, the PET machanism is not the only fluorescence quenching mechanism, since the F_0/F (2.95) versus Cu^{2+} (1 μM) was much higher than that of τ_0/τ (1.04). As shown in Figure S9, a new absorption spectrum at 265 nm was appeared when Cu^{2+} was added into the P, O-g-C_3N_4 nanodots and the absorbance increased with the increase of Cu^{2+} concentration. This implied the formation of P, O-g-C_3N_4 nanodots-Cu^{2+} complex and that the static

fluorescence quenching is another predominant fluorescence quenching mechanism. Moreover, we found that ethylenediaminetetraacetic acid (EDTA), a strong Cu^{2+} chelator, could effectively restore the fluorescence of the P, O-g-C_3N_4 nanodots-Cu^{2+} system (Figure 4A), which implied that the interaction between the P, O-g-C_3N_4 nanodots and Cu^{2+} is reversible.

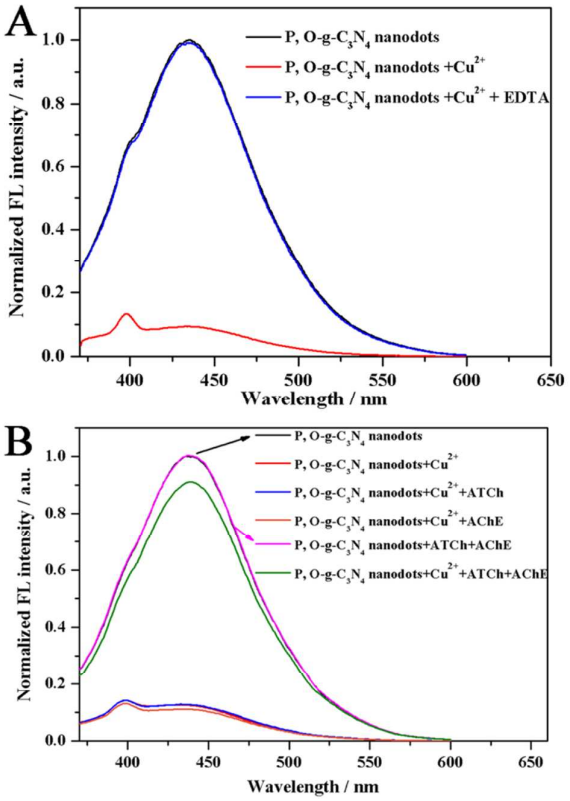

Figure 4. (A) Fluorescence responses of the P, O-g-C_3N_4 nanodots in the presence of Cu^{2+}, Cu^{2+} and EDTA in 10 mM borate buffer (pH 7.0); the concentration of Cu^{2+} and EDTA was 15 μM. (B) Fluorescence responses of the P, O-g-C_3N_4 nanodots in the presence of Cu^{2+}, Cu^{2+} and ATCh, Cu^{2+} and AChE; both ATCh and AChE and all of Cu^{2+}, ATCh and AChE were in 10 mM borate buffer (pH 7.0); the concentrations of Cu^{2+}, ATCh and AChE were 15 μM, 1 mM and 10 mU/mL.

Fluorescence determination of the P, O-g-C_3N_4 nanodots-Cu^{2+} towards AChE activity

The reversible interaction and the restored fluorescence of the P, O-g-C_3N_4

nanodots and Cu^{2+} reminded us of the potential applications of the system in the detection of other chalcophile substances. Bearing this in mind, we explored its application in enzymatic activity assay. In the sensing mechanism as illustrated in Scheme 1B, ATCh is an analogue of acetylcholine and a substrate of AChE, and it can be efficiently hydrolyzed into TCh by AChE. Just like the well-known reaction of Cu and mercaptans, TCh can react with Cu^{2+} to form a Cu(I)-TCh complex.[26] The binding force of Cu^{2+} and TCh is stronger than that of Cu^{2+} and the P, O-g-C_3N_4 nanodots and, as a result, the fluorescence of the P, O-g-C_3N_4 nanodots-Cu^{2+} system would gradually be restored with the increase of AChE. To confirm this idea, we investigated the feasibility of the proposed approach. As shown in Figure 4B, the AChE-catalyzed reaction with ATCh as a substrate caused an obvious fluorescence intensity enhancement of the P, O-g-C_3N_4 nanodots-Cu^{2+} complex compared to that without AChE (nearly 90% fluorescence restored compared to the P, O-g-C_3N_4 nanodots), and neither ATCh nor AChE caused remarkable fluorescence restoration. The optimal incubation time and concentration of ATCh to complete the hydrolysis were found to be 30 min and 1 mM (Figures S10 and S11). Under optimal conditions, the dynamic responses of AChE were recorded by the fluorescence responses of the P, O-g-C_3N_4 nanodots. With the gradual hydrolysis of ATCh, the fluorescence of the P, O-g-C_3N_4 nanodots continually increased, with the concentration of AChE increasing from 0 to 20 mU/mL, and reached a plateau at 10 mU/mL (Figures 5A and 5B). A linearity range from 0.01 to 3.0 mU/mL was obtained with a detection limit of 0.01 mU/mL. This was very sensitive compared with many previous reports (Table S3). In order to evaluate the selectivity of the proposed approach towards the detection of AChE activity, we chose some co-existing substances, including various enzymes and proteins, small thiol molecules and ions. As seen in Figure 5C, non-specific enzymes and other interferences could induce a remarkable fluorescence response as AChE was presented. This result confirmed the efficiency of the proposed method for the determination of AChE activity.

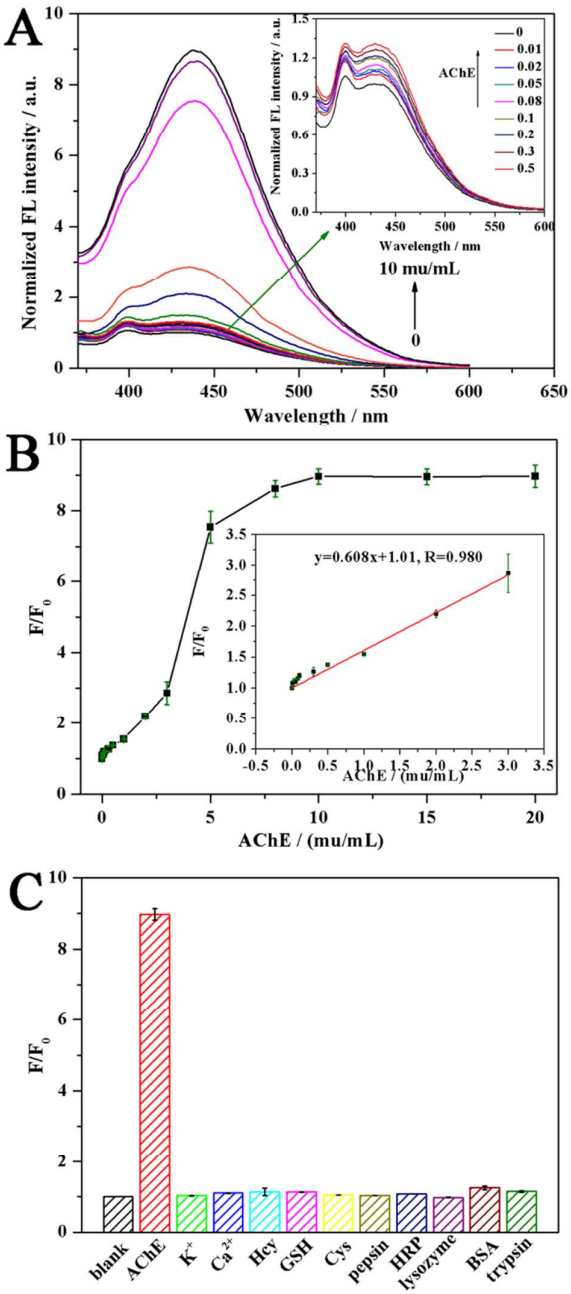

Figure 5. (A) Fluorescence responses of the P, O-g-C_3N_4 nanodots in the presence of 15 μM Cu^{2+} and different concentrations of AChE (0, 0.01, 0.02, 0.05, 0.08, 0.1, 0.2, 0.3, 0.5, 1, 2, 3, 5, 8, 10, 15, 20 mU/mL) in 10 mM borate buffer (pH 7.0). The inset figure presents the fluorescence responses of the P, O-g-C_3N_4 nanodots with 15 μM Cu^{2+} at low concentrations of AChE. (B) The relationship between F_0/F and the concentration of AChE. The inset figure presents the linear responses to AChE ranging from 0.01 to 3 mU/mL. (C) Fluorescence responses of the P, O-g-C_3N_4 nanodots in the presence of 15 μM Cu^{2+} and other interference solutions. F_0 and F represent the fluorescence intensities of the P, O-g-C_3N_4 nanodots with 15 μM Cu^{2+} at 440 nm in the absence and presence of AChE or other interference solutions.

In addition, the application of the proposed method was investigated in the determination of AChE activity in human plasma. The concentration of AChE activity of the diluted human plasma was determined using our method. In the determination, obvious fluorescence enhancement could be observed for the P, O-g-C_3N_4 nanodots-Cu^{2+} system, implying the potential applicability of the proposed method to biological fluid samples. (Table 2)

Table 2. Determination of AChE activity in diluted human plasma samples (n=3)

Samples (human plasma)	Concentration found (mU/mL)	RSD %
1	1.22	1.52
2	1.53	2.13

Conclusions

In this study, highly fluorescent P, O-g-C_3N_4 nanodots were synthesized using chemical oxidation and hydrothermal etching of bulk P-g-C_3N_4 obtained via pyrolysis of phytic acid and melamine. Using the fluorescent P, O-g-C_3N_4 nanodots, an effective and facile fluorescence approach was developed for the sensitive and selective determination of Cu^{2+} and AChE activity in aqueous solutions. Under optimal conditions, a rapid fluorescence turn off detection for Cu^{2+} could be completed in 5 min with a detection limit of 2 nM, independent of other metal ions. Furthermore, using ATCh as a substrate, the fluorescence of the P, O-g-C_3N_4 nanodots-Cu^{2+} system could be remarkably restored, and it could be used in the sensitive detection of AChE activity through the reaction between Cu^{2+} and TCh (the hydrolysis product of ATCh) with a detection limit of 0.01 mU/mL. In addition, the proposed approach showed potential application for detection of Cu^{2+} in natural water samples, and the AChE activity in human plasma.

Acknowledgements

This research work was financially supported by the National Nature Scientific Foundation of China (No. 21375112，No. 21521004) and Program of Science and Technology of Xiamen for University Innovation (3502Z20143025), which are gratefully acknowledged. Furthermore, we would like to extend our thanks to Professor John Hodgkiss of The University of Hong Kong for his assistance with English.

References

1. Y. Wang, X. Wang and M. Antonietti, *Angew Chem Int Ed*, 2012, 51, 68-89.
2. Y. Zheng, Y. Jiao, M. Jaroniec, Y. Jin and S. Z. Qiao, *Small*, 2012, 8, 3550-3566.
3. J. Xu, T. J. Brenner, L. Chabanne, D. Neher, M. Antonietti and M. Shalom, *J. Am. Chem. Soc.,* 2014, 136, 13486-13489.
4. S. Cao, J. Low, J. Yu and M. Jaroniec, *Adv Mater*, 2015, 27, 2150-2176.
5. N. Cheng, J. Tian, Q. Liu, C. Ge, A. H. Qusti, A. M. Asiri, A. O. Al-Youbi and X. Sun, *ACS appl. Mater. Interfaces*, 2013, 5, 6815-6819.
6. Y. Tang, Y. Su, N. Yang, L. Zhang and Y. Lv, *Anal. Chem.,* 2014, 86, 4528-4535.
7. J. Tian, Q. Liu, A. M. Asiri, A. O. Al-Youbi and X. Sun, *Anal. Chem.,* 2013, 85, 5595-5599.
8. N. Cheng, P. Jiang, Q. Liu, J. Tian, A. M. Asiri and X. Sun, *Analyst*, 2014, 139, 5065-5068.
9. X. Zhang, X. Xie, H. Wang, J. Zhang, B. Pan and Y. Xie, *J. Am. Chem. Soc.,* 2013, 135, 18-21.
10. X. Zhang, H. Wang, Q. Zhang, J. Xie, Y. Tian, J. Wang and Y. Xie, *Adv Mater*, 2014, 26, 4438-4443.
11. J. Tian, Q. Liu, A. M. Asiri, A. H. Qusti, A. O. Al-Youbi and X. Sun, *Nanoscale*, 2013, 5, 11604-11609.
12. J. Tian, Q. Liu, C. Ge, Z. Xing, A. M. Asiri, A. O. Al-Youbi and X. Sun, *Nanoscale*, 2013, 5, 8921-8924.
13. S. Liu, J. Tian, L. Wang, Y. Luo and X. Sun, *RSC Adv.*, 2012, 2, 411-413.
14. M. Rong, L. Lin, X. Song, T. Zhao, Y. Zhong, J. Yan, Y. Wang and X. Chen, *Anal. Chem.,* 2015, 87, 1288-1296.
15. Y.-C. Lu, J. Chen, A.-J. Wang, N. Bao, J.-J. Feng, W. Wang and L. Shao, *J. Mater. Chem. C*, 2015, 3, 73-78.
16. J. Shen, Y. Li, Y. Su, Y. Zhu, H. Jiang, X. Yang and C. Li, *Nanoscale*, 2015, 7, 2003-2008.
17. S. Zhang, J. Li, M. Zeng, J. Xu, X. Wang and W. Hu, *Nanoscale*, 2014, 6, 4157-4162.
18. S. Barman and M. Sadhukhan, *J. Mater. Chem.,* 2012, 22, 21832.
10. Z. Lin and X. Wang, *Angew Chem Int Ed*, 2013, 52, 1735-1738.
20. J. Li, B. Shen, Z. Hong, B. Lin, B. Gao and Y. Chen, *Chem Commun*, 2012, 48,

12017-12019.
21. H. Wang, X. Zhang, J. Xie, J. Zhang, P. Ma, B. Pan and Y. Xie, *Nanoscale*, 2015, 7, 5152-5156.
22. T. Y. Ma, J. Ran, S. Dai, M. Jaroniec and S. Z. Qiao, *Angew Chem Int Ed*, 2015, 54, 4646-4650.
23. X. Bai, C. Sun, S. Wu and Y. Zhu, *J. Mater. Chem. A*, 2015, 3, 2741-2747.
24. Q. Han, C. Hu, F. Zhao, Z. Zhang, N. Chen and L. Qu, *J. Mater. Chem. A*, 2015, 3, 4612-4619.
25. M. Vedamalai, A. P. Periasamy, C. W. Wang, Y. T. Tseng, L. C. Ho, C. C. Shih and H. T. Chang, *Nanoscale*, 2014, 6, 13119-13125.
26. C. Lei, Z. Wang, Z. Nie, H. Deng, H. Hu, Y. Huang and S. Yao, *Anal. Chem.,* 2015, 87, 1974-1980.
27. N. Zhang, Y. Si, Z. Sun, L. Chen, R. Li, Y. Qiao and H. Wang, *Anal. Chem.,* 2014, 86, 11714-11721.
28. L. H. Jin and C. S. Han, *Anal. Chem.,* 2014, 86, 7209-7213.
29. P. Li, X. Duan, Z. Chen, Y. Liu, T. Xie, L. Fang, X. Li, M. Yin and B. Tang, *Chem Commun*, 2011, 47, 7755-7757.
30. D. L. Ma, H. Z. He, D. S. Chan, C. Y. Wong and C. H. Leung, *PloS one*, 2014, 9, e99930-e99937.
31. M. Wang, K. H. Leung, S. Lin, D. S. Chan, D. W. Kwong, C. H. Leung and D. L. Ma, *Scientific reports*, 2014, 4, 6794-6800.
32. T. He, L. Qi, J. Zhang, Y.-L. Huang and Z.-Q. Zhang, *Sens. Actuators, B*, 2015, 215, 24-29.
33. S. Liao, W. Han, H. Ding, D. Xie, H. Tan, S. Yang, Z. Wu, G. Shen and R. Yu, *Anal. Chem.,* 2013, 85, 4968-4973.
34. Q. Long, H. Li, Y. Zhang and S. Yao, *Biosens. Bioelectron.,* 2015, 68, 168-174.
35. G. Garai-Ibabe, L. Saa and V. Pavlov, *The Analyst*, 2014, 139, 280-284.
36. K. Ma, L. Lu, Z. Qi, J. Feng, C. Zhuo and Y. Zhang, *Biosens. Bioelectron.,* 2015, 68, 648-653.
37. M. Shalom, S. Inal, C. Fettkenhauer, D. Neher and M. Antonietti, *J. Am. Chem. Soc.,*2013, 135, 7118-7121.
38. B. Samotus and S. Schwimmer, *Nature*, 1962, 194, 578-579.
39. M. Rong, L. Lin, X. Song, Y. Wang, Y. Zhong, J. Yan, Y. Feng, X. Zeng and X. Chen, *Biosens. Bioelectron.,* 2015, 68, 210-217.
40. Y. Zhang and M. Antonietti, *Chemistry, an Asian journal*, 2010, 5, 1307-1311.
41. Y. Zhou, L. Zhang, J. Liu, X. Fan, B. Wang, M. Wang, W. Ren, J. Wang, M. Li and J. Shi, *J. Mater. Chem. A*, 2015, 3, 3862-3867.
42. P. Yang, J. Zhao, J. Wang, B. Cao, L. Li and Z. Zhu, *J. Mater. Chem. A*, 2015, 3, 136-138.
43. Y. Zhang, Q. Pan, G. Chai, M. Liang, G. Dong, Q. Zhang and J. Qiu, *Scientific reports*, 2013, 3, 1943.
44. D. Pan, J. Zhang, Z. Li and M. Wu, *Adv Mater*, 2010, 22, 734-738.
45. L. Lin, M. Rong, S. Lu, X. Song, Y. Zhong, J. Yan, Y. Wang and X. Chen, *Nanoscale*, 2015, 7, 1872-1878.

46. B. B. Wang, Q. J. Cheng, L. H. Wang, K. Zheng and K. Ostrikov, *Carbon*, 2012, 50, 3561-3571.
47. C. Cheng, Y. Huang, X. Tian, B. Zheng, Y. Li, H. Yuan, D. Xiao, S. Xie and M. M. Choi, *Anal. Chem.,* 2012, 84, 4754-4759.
48. H. Xu, J. Yan, X. She, L. Xu, J. Xia, Y. Xu, Y. Song, L. Huang and H. Li, *Nanoscale*, 2014, 6, 1406-1415.

Graphical abstract